Digital In-Line Holography System for 3D-3C Particle Tracking Velocimetry

Mokrane Malek[1], Denis Lebrun[2], and Daniel Allano[2]

[1] UMR A 1114 Climate, Soil, Environment,
University of Avignon,
33, rue Louis Pasteur,
84000 Avignon, France
mokrane.malek@univ-avignon.fr
[2] UMR 6614 CORIA,
Université de Rouen,
76801 Saint Etienne du Rouvray, France
lebrun@coria.fr

Abstract. Digital in-line holography is a suitable method for measuring three dimensional (3D) velocity fields. Such a system records directly on a charge-coupled device (CCD) camera a couple of diffraction patterns produced by small particles illuminated by a modulated laser diode. The numerical reconstruction is based on the wavelet transformation method. A 3D particle field is reconstructed by computing the wavelet components for different scale parameters. The scale parameter is directly related to the axial distance between a given particle and the CCD camera. The particle images are identified and localized by analyzing the maximum of the wavelet transform modulus (WTMM) and the equivalent diameter of the particle image (D_{eq}). Afterwards, a 3D point-matching (PM) algorithm is applied to the pair of sets containing the 3D particle locations. In the PM algorithm, the displacement of the particles is modeled by an affine transformation. This affine transformation is based on the use of the dual number quaternions. Afterwards, the velocity-field extraction is performed. This system is tested with simulated particle field displacements and the feasibility is checked with an experimental displacement.

1 Introduction

Recently, we have demonstrated that digital in-line holography can be used to determine 2D velocity fields in several slices of a sample volume [1]. In-line holograms record on a CCD camera the far-field diffraction patterns of particles so that a large field can be stored. Then, from the reconstructed sample volume, the 3D location and size of each particles can be determined [2]. This technique constitutes an alternative to classical particle-field holography [3–9].

Generally, the diffraction pattern is analyzed by means of space-frequency operators. For example, *Onural* [10] showed that the diffraction process can be seen as a convolution operation between the amplitude transmission in the space plane and a family of wavelet functions. In a similar way, the holographic reconstruction process can be seen as a wavelet transform (WT)

A. Schroeder, C. E. Willert (Eds.): Particle Image Velocimetry,
Topics Appl. Physics **112**, 155–170 (2008)

of the hologram transmission function. More recently, it has been shown that the fractional fourier transformation (FRFT) was well adapted to carry out a digital reconstruction of near-field holograms [11, 12].

In this chapter, we show that in-line holography can be extended to determine 3D velocity fields in a flow that contains particle tracers. By this technique, we record directly on a charge coupled device (CCD) camera a couple of diffraction patterns produced from small particles illuminated by a modulated laser diode. The numerical reconstruction is achieved by applying the wavelet transformation method. The determination of the velocity vector is based on two main steps. First, the 3D coordinates of each particle image within a predefined reconstructed volume are extracted. In the second step, a particle tracking velocimetry (PTV) based on a point-matching (PM) algorithm is applied to find the best correspondence between the two sets of particle positions.

In Sect. 2, the theoretical background used for digital in-line reconstruction of holograms is recalled. In Sect. 3, we present a description of the proposed method for the estimation of 3D coordinates of each particle by the analysis of the variations of WTMM and the D_{eq} of the reconstructed image. Then, the main objective of this section is devoted to the presentation of the algorithm used to find the best correspondence between particle images. In Sect. 4, this method is applied on simulated holograms. Then, experimental results about 3D displacements of particle fields attest that such an approach can provide an interesting tool for diagnostics in flows. Finally, the advantage and the limitation of the presented HPTV method are discussed.

2 Theoretical Background

Let us recall the digital reconstruction process proposed by authors of [9]. Consider an opaque object $O(\xi, \eta)$ of diameter d illuminated by a monochromatic plane wave (see Fig. 1). The intensity distribution on a plane (x, y) located at a distance z_0 from this object can be approximated by the following convolution operation:

$$I_{z_0}(x, y) = 1 - O(x, y) * * \frac{2}{\lambda z_0} \sin\left[\frac{\pi(x^2 + y^2)}{\lambda z_0}\right]. \tag{1}$$

Note here that the intermodulation term has been neglected. This simplification is valid in the general case of far-field in-line holography (i.e., $\pi d^2/\lambda z_0 \ll 1$). The expression given by (1) can be rewritten as a WT of the amplitude distribution in the object plane:

$$I_{z_0}(x, y) = 1 - \frac{2}{\pi} \mathrm{WT}_O(a_0, x, y). \tag{2}$$

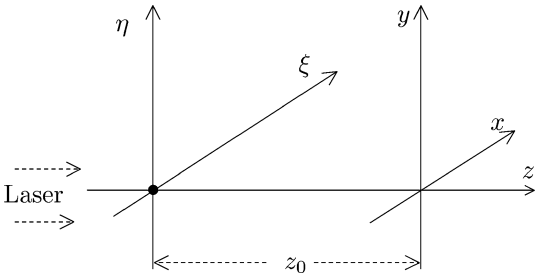

Fig. 1. Hologram recording in the Gabor configuration

The daughter wavelet functions are defined for the scale parameter a by:

$$\Psi_a = \frac{1}{a^2} \sin\left(\frac{x^2 + y^2}{a^2}\right). \tag{3}$$

The scale parameter a_0 of the wavelet is related to the distance z_0 as follows:

$$a_0 = \sqrt{\frac{\lambda z_0}{\pi}}. \tag{4}$$

In the same way, this approach can be used for hologram reconstruction. The reconstructed image at a given distance z_r can be seen as the WT of the intensity distribution recorded by the photosensitive plane. When $a_r = a_0 = a$ (i.e., the interrogation plane located at a distance z_r corresponds to the object plane located at a distance z_0), it can be shown that by dropping a multiplicative constant term:

$$\mathrm{WT}_{I_z}(a, x, y) = 1 - O(x, y) - \frac{1}{2\lambda z} O(x, y) * * \sin\left[\frac{\pi(x^2 + y^2)}{2\lambda z}\right]. \tag{5}$$

The object function $O(x, y)$ can be easily reconstructed. This method can be extended to the case of several particles of different diameters provided that the far-field condition is maintained.

In fact, the function given by (3) is not really a wavelet and must be modified in order to check the admissibility conditions of a wavelet function (zero mean and localization). It is shown [9] that the following function can be used:

$$\Psi_{\mathrm{Ga}}(x, y) = \frac{1}{a^2}\left[\sin\left(\frac{x^2 + y^2}{a^2}\right) - M_\Psi(\sigma)\right] \exp\left(-\frac{x^2 + y^2}{\sigma^2 a^2}\right), \tag{6}$$

where σ is a parameter that depends on the recording system (CCD camera) specifications. Its value is well discussed in [13]. The parameter M_Ψ is adjusted in order to have a zero mean value of $\Psi_{\mathrm{Ga}}(x, y)$.

3 3D Velocity Field Extraction and Data Postprocessing

In fluid flows studies, the analysis of the velocity in multiple planes or in a sample volume is of great interest. In our previous work we have demonstrated the feasibility of investigating several parallel planes by using digital in-line holography [1]. In this section we generalize this method to extract a 3D velocity field in a sample volume. The particle field to be studied is twice illuminated by a collimated laser beam emanating from a low-power modulated laser diode. When the object field to be studied is not too large, the diffraction patterns of particles can be directly recorded by means of a CCD camera. However, it should be admitted that generally an optical imaging setup with magnification under unity must be used so that larger image fields are both reported near the CCD camera. Compared to the equipment required in PIV experiments, this method has several advantages. Firstly, a low-power laser source is required and the same laser cavity is used to generate the two pulses. Such a source has been used successfully in a three-dimensional two-component (3D-2C) particle tracking velocimetry with a real flow [1]. Secondly, the in-line configuration is appreciated when optical access is limited.

In digital in-line holography, out-of-focus particle images give rise to high-contrast circular rings. Consequently, classical correlation-based algorithms (that are commonly used in PIV experiments) are not suitable for finding a local displacement of holographic particle images. Indeed, the displacement of out-of-focus images has the same influence on the correlation map as the infocus image displacements. Therefore, the mean velocity cannot be directly evaluated by using a statistical operator based on the gray-level analysis of the reconstructed images.

Our approach for velocity field analysis is based on two main steps. First, The 3D particle coordinates of each particle identified within a predefined reconstructed slice are extracted. The method used to validate a bright spot as a particle image is developed in the next section. In the second step, the point-matching algorithm is applied to find the best correspondence between the two sets of particle positions. This result is used to extract the 3D velocity field.

3.1 Extraction of 3D Particle Images

The computation of the velocity field from a couple of images gives rise to the need of a robust and accurate method for extracting particle coordinates from the reconstructed 3D images.

First, let us consider a space region corresponding to a set of reconstructed z-planes $WT_{I_z}(a, x, y)$ such that the inequalities $z_\mathrm{r} - \delta z \leq z \leq z_\mathrm{r} + \delta z$ are checked. This region defines a sample volume built from several reconstructed planes and whose thickness is equal to $2\delta z$ (typically a few millimeters).

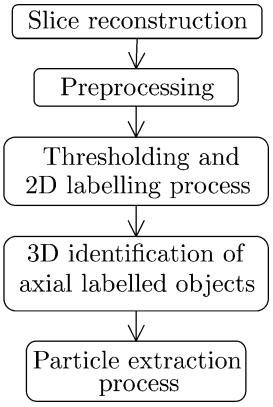

Fig. 2. General process for determining the 3D particles's locations

The general process to determine the 3D particle locations within this volume is outlined in Fig. 2.

Before selecting the supposed particle images by a thresholding operation, a background substraction is performed. The background is estimated by using a morphological opening operator. The size of the structuring element of this operator must be much higher than the particle-image diameters. The objective of this operation is to improve the signal-to-noise ratio by enhancing the contrast of the particle images in each plane. This operation is followed by a thresholding and a 2D labeling operations. Then, the x–y positions of labeled objects in each plane are available.

In the fourth step, a 3D labeled object is built by clustering the 2D labeled objects located on the same z-axis. During this operation, only the 3D labeled objects that are contained at least in three consecutive planes are considered as particle images. The use of this rejection principle is based on the great depth of field property of in-line holographic images. Therefore, a given labelled particle image is inevitably detected in several adjacent z-planes (see Fig. 3).

Finally, the result of the above step is used for recognizing the particles among all the three-dimensional labeled objects in the slice by using both the wavelet transform maximum modulus (WTMM) and the equivalent diameter (D_{eq}) variations versus the reconstruction distance z_{r}.

The WTMM method has been proposed in [14] to estimate the axial location of the particle images. The best focus plane is supposed to be the axial distance that gives the maximum of WTMM(z_{r}). The use of the $D_{\mathrm{eq}}(z_{\mathrm{r}})$ has been proposed in [15] to evaluate particle location. It can be shown that the axial position of the particle corresponds to a minimum of D_{eq} (see Fig. 4). Let us consider Z_1 and Z_2 as the axial coordinates corresponding, respectively, to the maximum of WTMM(z_{r}) and the minimum of $D_{\mathrm{eq}}(z_{\mathrm{r}})$. The joint exploitation of these extrema efficiently eliminates ambiguities between the 3D particle images and other 3D objects that are present in several planes.

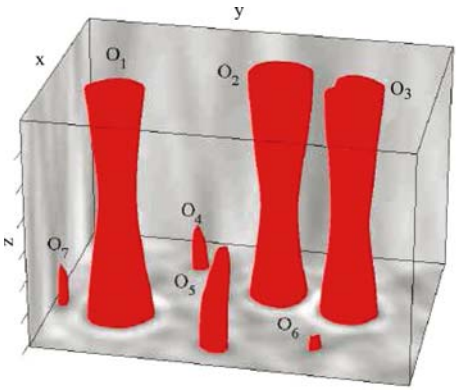

Fig. 3. An isosurface computed from the constructed sample volume containing 3 particle images (3D objects denoted O_1, O_2 and O_3)

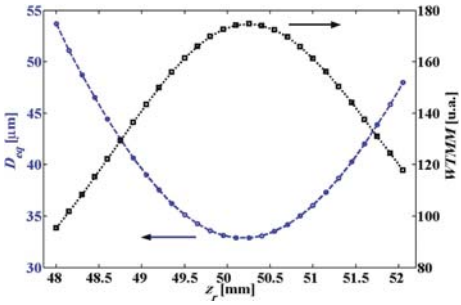

Fig. 4. Variations in WTMM and D_{eq} versus z_{r}

In the actual sample volume, only the 3D labeled objects that present the parabolic shapes of the WTMM and D_{eq} curves (as shown in Fig. 4) and that check $Z_1 \approx Z_2$ are considered as 3D particle images. In the example illustrated in Fig. 3, only 3D objects denoted O_1, O_2 and O_3 are considered as particle images.

3.2 Computation of the 3D Velocity Field

3.2.1 Dual-Number Quaternion for 3D Pose Estimation

In this section we recall the properties of dual-number quaternions as proposed in [16]. Quaternions are an extension of complex numbers to R^4 that consist of a 3×1 vector and a scalar component. Formally, a quaternion $\boldsymbol{q}$ can be defined as

$$\boldsymbol{q} = \begin{bmatrix} q_1 \\ q_2 \\ q_3 \\ q_4 \end{bmatrix} = \begin{bmatrix} \boldsymbol{q} \\ q_4 \end{bmatrix} . \tag{7}$$

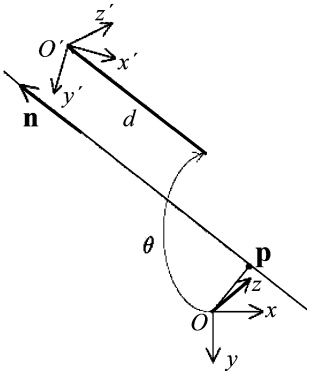

Fig. 5. Rotation and translation by using dual-number quaternion

In this chapter, each quaternion is represented by a bold-face italic character (for example $\boldsymbol{q}$) and all 3×1 vector by a standard bold-face character (for example $\mathbf{q}$).

Quaternions are limited to representing 3D rotation. In this case, the components of a quaternion are called the Euler symmetric parameters and we can rewrite the expression of the quaternion as

$$\boldsymbol{q} = \begin{bmatrix} \sin(\theta/2)\mathbf{n} \\ \cos(\theta/2) \end{bmatrix} . \tag{8}$$

The unit vector $\mathbf{n}$ is the vector about which the coordinate system has rotated and θ is the amount of rotation about $\mathbf{n}$.

By using $\mathbf{q}$ and q_4 the rotation matrix is expressed as

$$\mathbf{R} = (q_4^2 - \mathbf{q}^T\mathbf{q})\mathbf{I} + \mathbf{q}\mathbf{q}^T + 2q_4\mathbf{K}(\mathbf{q}) , \tag{9}$$

where

$$\boldsymbol{K}(\mathbf{q}) = \begin{bmatrix} 0 & -q_3 & q_2 \\ q_3 & 0 & -q_1 \\ -q_2 & q_1 & 0 \end{bmatrix} . \tag{10}$$

$\boldsymbol{I}$ is 4×4 identity matrix.

To represent both rotation and translation at the same time we can use the dual-number quaternions. These numbers consist of two parts,

$$\widehat{\boldsymbol{q}} = \boldsymbol{r} + \epsilon\, \boldsymbol{s} , \tag{11}$$

where $\boldsymbol{r}$ and $\boldsymbol{s}$ are quaternions and are called the real part and dual part of $\widehat{\boldsymbol{q}}$ and $\epsilon^2 = 0$.

By this representation, a given 3D transformation can be described by first translating the original coordinate frame along the direction of unit vector $\mathbf{n}$ by the distance d and then by rotating it by an angle θ around the line having $\boldsymbol{n}$ as unit vector and passing through a point $\mathbf{p}$ (see Fig. 5). The quaternions

$\boldsymbol{r}$ and $\boldsymbol{s}$ are related to the screw parameters ($\mathbf{n}$, θ and $\mathbf{p}$) by the following equations:

$$\boldsymbol{r} = \begin{bmatrix} \sin(\theta/2)\mathbf{n} \\ \cos(\theta/2) \end{bmatrix} \tag{12}$$

and

$$\boldsymbol{s} = \begin{bmatrix} \frac{d}{2}\cos(\theta/2)\mathbf{n} + \sin(\theta/2)(\mathbf{p} \times \mathbf{n}) \\ \cos(\theta/2) \end{bmatrix} . \tag{13}$$

Note that $\boldsymbol{r}$ and $\boldsymbol{s}$ must satisfy the following constraints:

$$\boldsymbol{r}^T \boldsymbol{r} = 1 \tag{14}$$

and

$$\boldsymbol{r}^T \boldsymbol{s} = 0 . \tag{15}$$

From the dual-quaternion representation of the 3D transform we can compute the homogeneous transform. The rotation matrix $\mathbf{R}$ can be deduced from the following expression:

$$\boldsymbol{R} = \begin{bmatrix} \mathbf{R} & 0 \\ \mathbf{0}^T & 1 \end{bmatrix} = \boldsymbol{W}(\boldsymbol{r})^T \boldsymbol{Q}(\boldsymbol{r}) , \tag{16}$$

where $\boldsymbol{W}(\boldsymbol{r})$ and $\boldsymbol{Q}(\boldsymbol{r})$ are defined as

$$\boldsymbol{W}(\boldsymbol{r}) = \begin{bmatrix} r_4 \boldsymbol{I} + \boldsymbol{K}(\boldsymbol{r}) & \boldsymbol{r} \\ -\boldsymbol{r}^T & r_4 \end{bmatrix} \tag{17}$$

and

$$\boldsymbol{Q}(\boldsymbol{r}) = \begin{bmatrix} r_4 \boldsymbol{I} - \boldsymbol{K}(\boldsymbol{r}) & \boldsymbol{r} \\ -\boldsymbol{r}^T & r_4 \end{bmatrix} . \tag{18}$$

The $\mathbf{0}^T$ is a 1×3 vector where all elements are equal to zero: $\mathbf{0}^T = [000]$.
The matrix $\boldsymbol{K}(r)$ is defined by (10).
The translation vector ($\mathbf{t}$) is related to the translation quaternion ($\boldsymbol{t}$) by

$$\mathbf{t} = \begin{bmatrix} \boldsymbol{t} \\ 0 \end{bmatrix} = \boldsymbol{W}(\boldsymbol{r})^T \boldsymbol{s} . \tag{19}$$

The full 3D affine transformation is represented here by $T_{[\boldsymbol{r},\boldsymbol{s}]}$ which consists of a rotation $\boldsymbol{R}$ followed by a translation $\boldsymbol{t}$.

3.2.2 Three-Dimensional Point-Matching Algorithm

In this section we present the formulation of our optimization problem by using dual-number quaternions for reaching the best correspondence between particle images of the first and the second exposure.

Firstly, both of the reconstructed sample volume are divided into 3D interrogation cells (IC). Let us consider that each IC consists of two frames X (taken at $t = t_0$), and Y (taken at $t = t_0 + \Delta t$), obtained from a double-exposure HPTV experiment. Such frames contain the two lists $\{\boldsymbol{X}_j, j = 1, \ldots, J\}$, and $\{\boldsymbol{Y}_k, k = 1, \ldots, K\}$ of the 3D particles' coordinates extracted as explained in Sect. 3.1. X is supposed to be related to Y by an affine transformation $T_{[\boldsymbol{r},\boldsymbol{s}]}$ defined below. The correspondence between particle j in the first set and particle k in the second set is defined by the correspondence variables m_{kj} that constitute the match-matrix $\boldsymbol{M}$ where

$$m_{kj} = \begin{cases} 1, & \text{if point } Y_k \text{ corresponds to point } X_j; \\ 0, & \text{otherwise.} \end{cases} \tag{20}$$

m_{kj} must satisfy the following equality constraints [17]:

$$\begin{aligned} m_{k(J+1)} + \sum_{j=1}^{j=J} m_{kj} &= 1\,, \\ m_{(K+1)j} + \sum_{k=1}^{k=K} m_{kj} &= 1\ . \end{aligned} \tag{21}$$

The elements $m_{k(J+1)}$ and $m_{(K+1)j}$ are added to interpret the missing particles. These variables are set to one if an error occurs during the extraction of positions from the reconstructed image or if a given particle image leaves the IC or enters in the IC.

By estimating the matrix $\boldsymbol{M}$ and the transformation parameters $\boldsymbol{r}$ and $\boldsymbol{s}$, the velocity vectors can be deduced in the considered IC.

Now, the problem is to estimate the optimal value of the $\boldsymbol{M}$, $\boldsymbol{r}$ and $\boldsymbol{s}$. The method used here consists in minimizing a cost function $E(\boldsymbol{M}, \boldsymbol{r}, \boldsymbol{s})$. According to reference [18], the form of E$(\boldsymbol{M}, \boldsymbol{r}, \boldsymbol{s})$ used in this work is:

$$\begin{aligned} E(\boldsymbol{M}, \boldsymbol{r}, \boldsymbol{s}) = \sum_{k=1}^{k=K} \sum_{j=1}^{j=J} m_{kj} \|\boldsymbol{Y}_k - T_{[\boldsymbol{r},\boldsymbol{s}]}(\boldsymbol{X}_j)\|^2 \\ + \alpha \left[\sum_{j=1}^{j=J} m_{(K+1)j} + \sum_{k=1}^{k=K} m_{k(J+1)} \right]. \end{aligned} \tag{22}$$

By using (16) and (19) the expression of $T_{[\boldsymbol{r},\boldsymbol{s}]}(\boldsymbol{X}_j)$ is:

$$T_{[\boldsymbol{r},\boldsymbol{s}]}(\boldsymbol{X}_j) = \boldsymbol{W}(\boldsymbol{r})^T \boldsymbol{s} + \boldsymbol{W}(\boldsymbol{r})^T \boldsymbol{Q}(\boldsymbol{r}) \boldsymbol{X}_j\,. \tag{23}$$

Note that here we use the quaternion representation of particle positions:

$$\boldsymbol{Y}_k = \frac{1}{2} \begin{bmatrix} \mathbf{Y}_k \\ 0 \end{bmatrix} \tag{24}$$

and

$$\mathbf{X}_j = \frac{1}{2}\begin{bmatrix} \boldsymbol{X}_j \\ 0 \end{bmatrix} . \tag{25}$$

The cost function $E(\boldsymbol{M}, \boldsymbol{r}, \boldsymbol{s})$ evaluates the degree of similarity between two sets of particle coordinates X and Y. The first term of this function is the sum of the assignment costs and the second represents the cost that incurred if a particle in one frame has no partner in the other frame. The α parameter is the cost of a no match and must satisfy the following inequality (see Sect. 2.1.3 of [18]):

$$\|\boldsymbol{Y}_k - T_{[\boldsymbol{r},\boldsymbol{s}]}(\boldsymbol{X}_j)\|^2 < \alpha . \tag{26}$$

By introducing the expression of $T_{[\boldsymbol{r},\boldsymbol{s}]}(\boldsymbol{X}_j)$ in (22) and using the properties $\boldsymbol{Q}(\boldsymbol{a})\boldsymbol{b} = \boldsymbol{W}(\boldsymbol{b})\boldsymbol{a}$ and $\boldsymbol{W}(\boldsymbol{a})^T\boldsymbol{W}(\boldsymbol{a}) = \boldsymbol{W}(\boldsymbol{a})\boldsymbol{W}(\boldsymbol{a})^T = \boldsymbol{a}^T\boldsymbol{a}\boldsymbol{I}$, the cost function can be written as a quadratic function of $\boldsymbol{r}$ and $\boldsymbol{s}$,

$$E(\boldsymbol{M}, \boldsymbol{r}, \boldsymbol{s}) = \boldsymbol{r}^T\boldsymbol{C}_1\boldsymbol{r} + \boldsymbol{s}^T\boldsymbol{C}_2\boldsymbol{s} + \boldsymbol{s}^T\boldsymbol{C}_3\boldsymbol{r} + \boldsymbol{C}_4 , \tag{27}$$

where

$$\begin{aligned}
\boldsymbol{C}_1 &= -2\sum_{k=1}^{k=K}\sum_{j=1}^{j=J} m_{kj}\boldsymbol{Q}^T(\boldsymbol{Y}_k)\boldsymbol{W}(\boldsymbol{X}_j) , \\
\boldsymbol{C}_2 &= \Big(\sum_{k=1}^{k=K}\sum_{j=1}^{j=J} m_{kj}\Big)\boldsymbol{I} , \\
\boldsymbol{C}_3 &= 2\sum_{k=1}^{k=K}\sum_{j=1}^{j=J} m_{kj}[\boldsymbol{W}(\boldsymbol{X}_j) - \boldsymbol{Q}(\boldsymbol{Y}_k)] , \\
\boldsymbol{C}_4 &= 2\sum_{k=1}^{k=K}\sum_{j=1}^{j=J} m_{kj}[\boldsymbol{X}_j^T\boldsymbol{X}_j + \boldsymbol{Y}_k^T\boldsymbol{Y}_k] \quad .
\end{aligned} \tag{28}$$

With this new representation, the cost function is minimized by the couple $(\widehat{\boldsymbol{r}}, \widehat{\boldsymbol{s}})$ where $\widehat{\boldsymbol{r}}$ is the eigenvector corresponding to the largest positive eigenvalue of matrix $\boldsymbol{A}$. $\boldsymbol{A}$ is defined by the following expression:

$$\boldsymbol{A} = \frac{1}{2}\boldsymbol{C}_3^T(\boldsymbol{C}_2 + \boldsymbol{C}_2^T)^{-1}\boldsymbol{C}_3 - \frac{1}{2}(\boldsymbol{C}_1 + \boldsymbol{C}_1^T) . \tag{29}$$

The knowledge of $\widehat{\boldsymbol{r}}$ enables us to calculate $\widehat{\boldsymbol{s}}$ by

$$\widehat{\boldsymbol{s}} = -(\boldsymbol{C}_2 + \boldsymbol{C}_2^T)^{-1}\boldsymbol{C}_3\widehat{\boldsymbol{r}} . \tag{30}$$

In order to find the optimal values for the correspondence matrix and the pose parameters, the cost function $E(\boldsymbol{M}, \boldsymbol{r}, \boldsymbol{s})$ is minimized with respect to its arguments. These optimal solutions are computed by using a 3D PM algorithm originally proposed by *Gold* et al. [17]. This algorithm has been

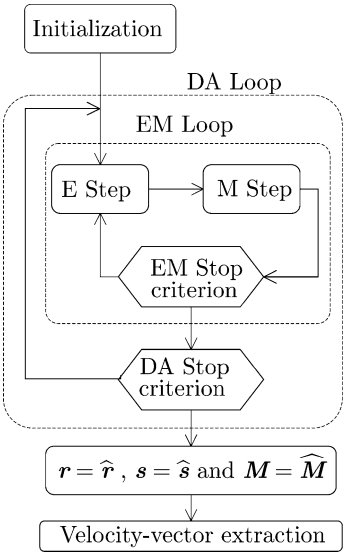

Fig. 6. Point-matching algorithm for 3D velocity-field extraction

extended by *Stellmacher* and *Obermayer* [18] for the development of a new particle tracking algorithm and by *Krepki* et al. [19] for the interrogation of 3D holographic PIV data.

As illustrated by Fig. 6, the solution of our optimization problem is realized by an expectation-minimization (EM) algorithm, which is combined with a deterministic annealing (DA) scheme. In the EM algorithm, we proceed in two steps. In the first step (M step) we estimate the correspondence matrix using the softassign algorithm [17]. This algorithm uses an iterative normalization along columns and rows with the exception of the slack variables. In the second step (E step) we estimate the pose parameters ($\boldsymbol{r}$, $\boldsymbol{s}$) using the dual-number quaternion method presented in Sect. 3.2.1. The whole EM algorithm is enclosed by a DA that is used to ensure convergence toward a global minimum of the cost function $E(\boldsymbol{M}, \boldsymbol{r}, \boldsymbol{s})$. The convergence of the DA scheme is governed by the inverse-temperature parameter β. This parameter can be selected between $\beta = \beta_{\text{begin}}$ (theoretically tends to zero) until $\beta = \beta_{\text{end}}$ (theoretically tends to $+\infty$) with an increment factor β_{fac}. In our case we have chosen $\beta_{\text{begin}} = 0.5$, $\beta_{\text{end}} = 1000$ and $\beta_{\text{fac}} = 1.5$. Finally, the velocity field is extracted by exploiting the correspondence matrix obtained. To improve this result we can use an adequate postprocessing as filtering and interpolation.

4 Simulations

In this section, we show the potentiality of the proposed method to evaluate the displacement according z-axis. We have simulated two intensity distribu-

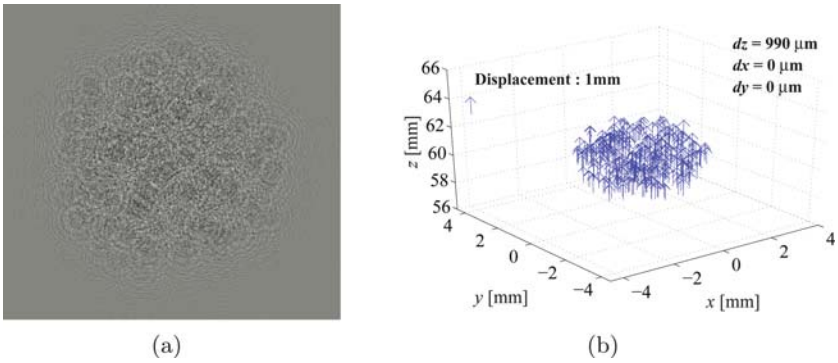

Fig. 7. 3D-3C HPTV: (**a**) Intensity distribution in one of the diffraction patterns and (**b**) reconstruction of the 3D velocity vector field

tions $I_1(x, y)$ and $I_2(x, y)$. These distributions are supposed to represent the diffraction patterns of the particle field at two different times. The concentration number in this simulation is set to 5 particles per mm^3 and the diameter of each particle is fixed to 20 µm. The particles are distributed uniformly in a spherical region with radius equal to 2.3 mm and center coordinate at ($x = 0$, $y = 0$, $z = 59.6$ mm). We have simulated a z-displacement by moving the particle field along the z-axis by 1 mm. Then, the pair of the reconstructed sample volumes is processed according to the procedure discussed in Sects. 3.1 and 3.2, respectively.

The result of this simulation is presented in Fig. 7. In this figure, dx, dy and dz are the average value of the measured displacement in x-, y-, and z-directions. As we can see, we have recovered the displacement vectors in the simulated sample volume. In this simulation, few false vectors have been produced. These vectors have been reduced by adjusting the parameters of the PM algorithm as the convergence criteria of the softassign algorithm, the EM algorithm and the DA.

The errors observed on the calculation of particle displacements are mainly due to the localization uncertainties during the extraction process. In fact, in a previous study we have established that the reliability of the extraction process depends on the signal-to-noise ratio (SNR) of the reconstructed particle fields [15]. We have shown that the particle number density should be drastically reduced for successful diagnostics in thick volume. Recall that the results presented in this simulation are obtained by a particle number density of 5 particles per mm^3. By using this low value, the error obtained on the measured z-displacement is 1 %.

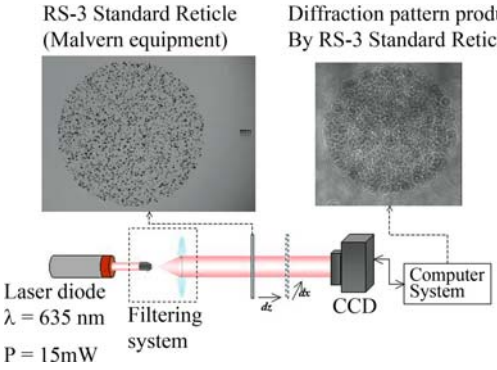

Fig. 8. Experimental setup for the 3D HPTV (z-axis and x-axis displacement: $d_z = 1\,\text{mm}$ and $d_x = 50\,\mu\text{m}$)

5 Experimental Results

In order to test our 3D HPTV system, we have used an RS-3 standard reticle (Malvern Equipment) that is approximately parallel to the recording plane. This reticle is an optical glass plate with a pattern of small opaque disks ($10\,\mu\text{m} < d < 90\,\mu\text{m}$) photographically deposited on the surface. This reticle is illuminated by a collimated laser beam generated by a low-power modulated laser diode ($P = 15\,\text{mW}$ and $\lambda = 635\,\text{nm}$).

The diffraction patterns corresponding to each exposure are both recorded by means of a CCD camera and digitized by a computer vision system as shown in Fig. 8. The size of the registered image is 1008×1018 pixels and the pixel size is equal to $9\,\mu\text{m}$.

At first, we have recorded one diffraction pattern generated by the reticle at a given position. Then, we have moved it by $1000\,\mu\text{m}$ in the z-direction and by $50\,\mu\text{m}$ in the x-direction. At this new position, a second diffraction pattern has been recorded.

Figure 9a shows an example of the diffraction pattern corresponding to one of the exposure. The information contained in this diffraction pattern leads to a satisfactory digital reconstruction. We have applied the process described in Sect. 3.1 to reconstruct the volume containing the particle field and to extract the 3D particle locations corresponding to each exposure. In this experiment, we have used the nearest-neighbor algorithm to reduce the level of miscalculation during the PM procedure. The reconstructed velocity vector map is presented in Fig. 9b. This result is obtained by applying a filtering process based on the analysis of the velocity histogram.

As shown by this figure, the average value of the measured displacement along the z-axis is $900\,\mu\text{m}$ (i.e., error of $10\,\%$). Here, the error is larger than in the simulation case. We believe that the experimental configuration causes a supplementary error. In fact, in this experiment, the displacements are realized manually. Thus, a systematic error is probably introduced into the

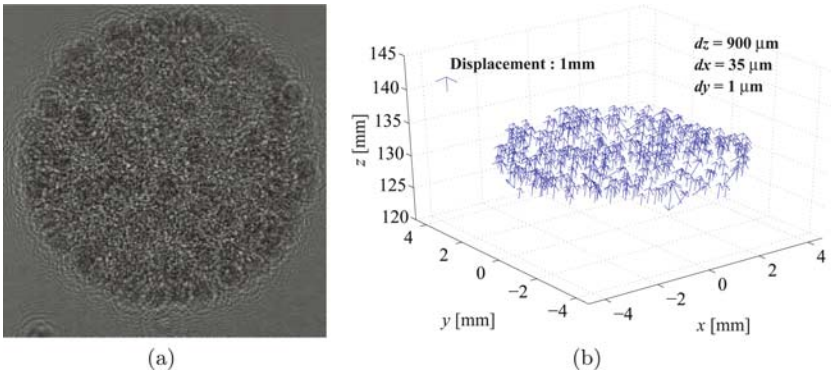

Fig. 9. Experimental result of 3D-3C HPTV: (**a**) Intensity distribution in one of the diffraction patterns and (**b**) reconstructed of 3D velocity vector

measurements. A second explanation concerning this difference is that the recording beam is not perfectly collimated. Consequently, a magnification factor less than unity could be introduced if a convergent beam was used.

Finally, some false vectors can be observed in Fig. 9b. These nonexpected vectors may significantly reduce the average value of the measured displacement.

These remarks are also valid for the difference observed in x- and y-directions.

According to the conclusion of [9], the best resolution that can be expected for the determination of the z-coordinate is about 50 µm when a plane wave illuminating a few particles is considered. More generally, when a higher particle concentration is considered, the accuracy in z can exceed more than several hundreds of micrometers.

Moreover, it must be noted that a uniform displacement has been used for testing our algorithm. Consequently, large IC ($128 \times 128 \times 128$) have been used. When small scales are investigated, for example in more complex two-plane flows, small IC are recommended. This point can be connected to the general problem of the spatial resolution in PIV experiment. Here, the discussion is extended in the 3D case.

6 Conclusion

In this study, it has been shown that the use of the digital in-line holography provides an appropriate tool to determine 3D velocity fields. This approach cannot be directly compared to other methods like particle image velocimetry (PIV) or laser Doppler velocimetry (LDV) where high-density seeding is recommended. Here, considering the limitations imposed by in-line holography, it is necessary to work with a low concentration of particles involved. Then 3D particle tracking velocimetry methods, based on the use of the point-matching algorithm, are more suited to this situation than correlation-based

methods. Although, the velocity vector fields are not statistically as reliable as those obtained by a PIV system, additional useful information concerning instantaneous velocity in a given 3D flow can be brought. Our experimental results show the feasibility and possibilities offered by this method.

References

[1] M. Malek, D. Allano, S. Coëtmellec, C. Özkul, D. Lebrun: Digital in-line holography for three-dimensional-two-components particle tracking velocimetry, Meas. Sci. Technol. **15**, 699–705 (2004) 155, 158

[2] G. A. Tyler, B. J. Thompson: Fraunhofer holography applied to particle size analysis a reassessment, Opt. Acta **23**, 685–700 (1976) 155

[3] T. M. Kreis, W. Jüptner: Suppression of the DC term in digital holography, Opt. Eng. **36**, 2357–2360 (1997) 155

[4] M. K. Kim: Tomographic three-dimensional imaging of a biological specimen using wavelength-scanning digital interference holography, Opt. Exp. **7**, 305–310 (2000) 155

[5] O. Schnars, W. Juptner: Direct recording of holograms by a CCD target and numerical reconstruction, Appl. Opt. **33**, 179–181 (1994) 155

[6] I. Yamaguchi, T. Zhang: Phase-shifting digital holography, Opt. Lett. **22**, 1268–1270 (1997) 155

[7] W. Xu, M. H. Jericho, H. J. Kreuzer, I. A. Meinertzhagen: Tracking particles in four dimensions with in-line holographic microscopy, Opt. Lett. **28**, 164–166 (2003) 155

[8] G. Pan, H. Meng: Tracking particles in four dimensions with in-line holographic microscopy, Appl. Opt. **42**, 827–833 (2003) 155

[9] C. Buraga-Lefebvre, S. Coëtmellec, D. Lebrun, C. Özkul: Application of wavelet transform to hologram analysis: Three-dimensional location of particles, Opt. Laser Eng. **33**, 409–421 (2000) 155, 156, 157, 168

[10] L. Onural: Diffraction from a wavelet point of view, Opt. Lett. **18**, 846–848 (1993) 155

[11] S. Coëtmellec, D. Lebrun, C. Özkul: Characterization of diffraction patterns directly from in-line holograms with the fractional fourier transform, App. Opt. **41**, 312–319 (2002) 156

[12] S. Coëtmellec, D. Lebrun, C. Özkul: Application of the two-dimensional fractional-orders fourier transformation to particle field digital holography, J. Opt. Soc. Am. A **19**, 1537–1546 (2002) 156

[13] M. Malek, S. Coëtmellec, D. Lebrun, D. Allano: Formulation of in-line holography process by a linear shift invariant system, Opt. Commun. **223**, 263–271 (2003) 157

[14] S. Belaïd, D. Lebrun, C. Özkul: Application of two dimensional wavelet transform to hologram analysis: Visualization of glass fibers in a turbulent flame, Opt. Eng. **36**, 1947–1951 (1997) 159

[15] M. Malek, D. Allano, S. Coëtmellec, D. Lebrun: Digital in-line holography influence of the shodow density on particle field extraction, Opt. Exp. **12**, 2270–2279 (2004) 159, 166

[16] M. W. Walker, L. Shao, R. A. Volz: Estimating 3-d location parameters using dual number quaternions, CVGIP:Image Understanding **54**, 358–367 (2004) 160

[17] S. Gold, C. P. Lu, A. Rangaragan, S. Pappu, E. Mjolsness: New algorithms for 2d and 3d point matching. pose estimation and correspondence, Pattern Recog. **31**, 1019–1031 (1998) 163, 164, 165
[18] M. Stellmacher, K. Obermayer: New particle tracking algorithm based on deterministic annealing and alternative distance measures, Exp. Fluids **28**, 506–518 (2000) 163, 164, 165
[19] B. Krepki, Y. Pu, H. Meng, K. Obermayer: A new algorithm for the interrogation of 3d holographic PTV data based on deterministic annealing and expectation minimization optimization, Exp. Fluids (Suppl.) **29**, S099–S0107 (2000) 165

Index